## Highlights

- Flexible *versus* rigid molecular structures of D-A-D type derivatives were synthesized.

- All compounds formed glasses with glass transition temperatures ranging from 92 to 131 ^{o}C.

- Their small ΔE_{ST} gaps ranged from 0.01 to 0.03 eV.

- The best hole and electron charge-transporting properties were observed for derivative **1**.

- OLED with *para*-donor-substituted diphenylsulfone as TADF emitter showed EQE of 24.1%.

Graphical abstract
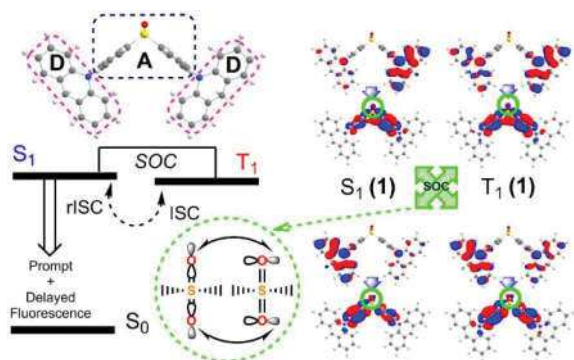
Flexible diphenylsulfone versus rigid dibenzothiophene dioxide as acceptor moieties in donor-acceptor-donor TADF emitters for highly efficient OLEDs

Dalius Gudeika[a,b], Jiun Haw Lee[c], Pei-Hsi Lee[c], Chia-Hsun Chen[c], Tien-Lung Chiu[d*], Glib V. Baryshnikov[e,f], Boris F. Minaev[e], Hans Ågren[e,g], Dmytro Volyniuk[a], Oleksandr Bezvikonnyi[a], Juozas V. Grazulevicius[a*]

[a] Department of Polymer Chemistry and Technology, Kaunas University of Technology, Radvilenu pl. 19, LT-50254, Kaunas, Lithuania

[b] Institute of Solid State Physics, University of Latvia, 8 Kengaraga St., Riga LV-1063, Latvia

[c] Graduate Institute of Photonics and Optoelectronics, National Taiwan University, 1, Section 4, Roosevelt Road, Taipei 10617, Taiwan

[d] Department of Electrical Engineering, Yuan Ze University, 135 Yuan-Tung Road, Taoyuan 32003, Taiwan

[e] Division of Theoretical Chemistry and Biology, School of Engineering Sciences in Chemistry, Biotechnology and Health, KTH Royal Institute of Technology, 10691, Stockholm, Sweden

[f] Department of Chemistry and Nanomaterials Science, Bohdan Khmelnytsky National University, 18031, Cherkasy, Ukraine

[g] College of Chemistry and Chemical Engineering, Henan University, Kaifeng, Henan 475004, P. R. China

Abstract

1

Flexible versus rigid molecular structures of donor-acceptor-donor type compounds are investigated with respect to efficiency of thermally activated delayed fluorescence (TADF) by theoretical and experimental approaches. Three highly efficient TADF emitters based on flexible diphenylsulfone and rigid dibenzothiophene dioxide as acceptor units and di-*tert*-butyldimethyldihydroacridine as donor moiety were designed and synthesized. Despite they showed similar singlet-triplet splitting (0.01-0.02 eV) and high photoluminescence quantum yields in appropriate hosts, maximum external quantum efficiencies as different as 24.1 and 15.9/19.4% were obtained for organic light emitting devices based on these emitters with, respectively, flexible and rigid molecular structures. The high efficiency of the light-emitting compounds with the flexible molecular structure could be traced to the bi-configurational nature of the lowest singlet and triplet states resulting in higher spin-orbit coupling than for molecules with rigid structures. All derivatives showed bipolar charge transport character. High device efficiency with electron mobility of 3×10^{-5} $cm^2V^{-1}s^{-1}$ and hole mobility of 1.3×10^{-4} $cm^2V^{-1}s^{-1}$ at the electric field of 5×10^5 Vcm^{-1} was recorded for the layer of *para*-disubstituted diphenylsulfone with flexible molecular structure. This TADF emitter showed an excellent performance in the organic light emitting device, exhibiting a maximum current efficiency, power efficiency, and external quantum efficiency of 61.1 cdA^{-1}, 64.0 lmW^{-1}, and 24.1%, respectively.

Keywords: Thermally activated delayed fluorescence, bipolar charge transport, dibenzothiophene dioxide, diphen-ylsulfone, di-*tert*-butyldimethyldihydroacridine.

1. **Introduction**

Organic light-emitting diodes (OLEDs) attract nowadays a great deal of attention for display and lighting applications [1-5]. The expanding OLED industry is on constant pursuit of new materials to level up the device performance, especially for blue emitter-based devices. Phosphorescence and thermally activated delayed fluorescence (TADF) are two well-known emission mechanisms which make it possible to achieve theoretical 100% internal quantum efficiency of OLEDs are [6-9]. Particularly, the latter mechanism has been much at focus as it does not require noble metal atoms in the molecular design [10]. In TADF based OLEDs under electrical pump, the statistical 75% triplet excitons up-convert to the singlet fluorescent level through reverse intersystem crossing (rISC). The rISC efficiency depends on several factors, most crucially on the energy difference (ΔE_{ST}) between the lowest singlet excited state (S_1) and triplet excited state (T_1), which also affects the overall device performance [11]. ΔE_{ST} can be flexibly adjusted by molecular design combining different donor and acceptor moieties [12,13]. Specially designed linear donor-acceptor-donor (D-A-D) compounds are thus widely used as highly efficient TADF emitters in OLEDs with state-of-art maximum external quantum efficiency [14-16]. Such TADF emitters have been synthesized using various donating moieties among of which the acridan unit is one showing excellent performance [17,18]. It has been shown that modification of hosts by *tert*-butyl units can lead to the blocking of energy-loss pathways of TADF emitters distributed in the host leading to enhancement of OLED efficiency [19]. "Full-exciton radiation" was achieved in TADF OLEDs using diphenylphosphine oxide as the secondary acceptor linked to *tert*-butylcarbazoles [20]. Direct attachment of *tert*-butyl groups to donating carbazole of D-A-D TADF emitters made it possible to increase device performance [21]. While *tert*-butylcarbazole moieties are widely utilized in TADF emitters [22], we have not

3

come across any examples of usage of the *tert*-butyl substituted acridan moiety donor unit in the design of TADF molecules. The selection of appropriate acceptor is evidently also a crucial point in the search for highly efficient TADF emitters. However, there is no established strategy so far for this selection.

Aiming to investigate the effect of rigidity of the acceptor on performance of TADF emitters in OLEDs, flexible diphenyl sulfone and rigid dibenzothiophene dioxide were selected as acceptor moieties in this work for the design of new TADF emitters containing *tert*-butylacridanyl group as upgraded donor unit. We here find that both the rigidity of the accepting units and *tert*-butyl modification of the donating units are significantly reflected on the efficiencies of the developed OLEDs. Electroluminescent devices with state-of-art maximum power efficiency of 64 lm·W^{-1} and maximum external quantum efficiency of 24.1% without outcoupling are demonstrated.

2. Results and discussion

2.1. *Synthesis and characterization*

Scheme 1 shows the synthetic pathway to compounds **1-3**. The intermediate compounds di(3-bromophenyl)sulfone (**II**), 2,8-dibromodibenzo[b,d]thiophene 5,5-dioxide (**III**) and 2,7-di-*tert*-butyl-9,9-dimethyl-9,10-dihydroacridine were synthesized as described elsewhere [23-25]. The target compound **1** was synthesized *via* a palladium-free nucleophilic cross-coupling reaction of bis(4-fluorophenyl)sulfone and 2,7-di-*tert*-butyl-9,9-dimethyl-9,10-dihydroacridine, whereas compounds **2** and **3** were prepared by palladium-catalyzed Buchwald-Hartwig cross-coupling reactions of 2,7-di-*tert*-butyl-9,9-dimethyl-9,10-dihydroacridine and di(3-bromophenyl)sulfone

or 2,8-dibromodibenzo[b,d]thiophene 5,5-dioxide, respectively. Derivatives **1-3** were purified by column chromatography and crystallization, and fully characterized using ^{1}H NMR, ^{13}C NMR spectroscopies, elemental analysis and mass spectrometry. The derivatives were soluble in dichlorobenzene, tetrahydrofuran (THF), chloroform, dioxane, ethylacetate and other organic solvents. The detailed information about the synthetic procedures are provided in Supporting Information.
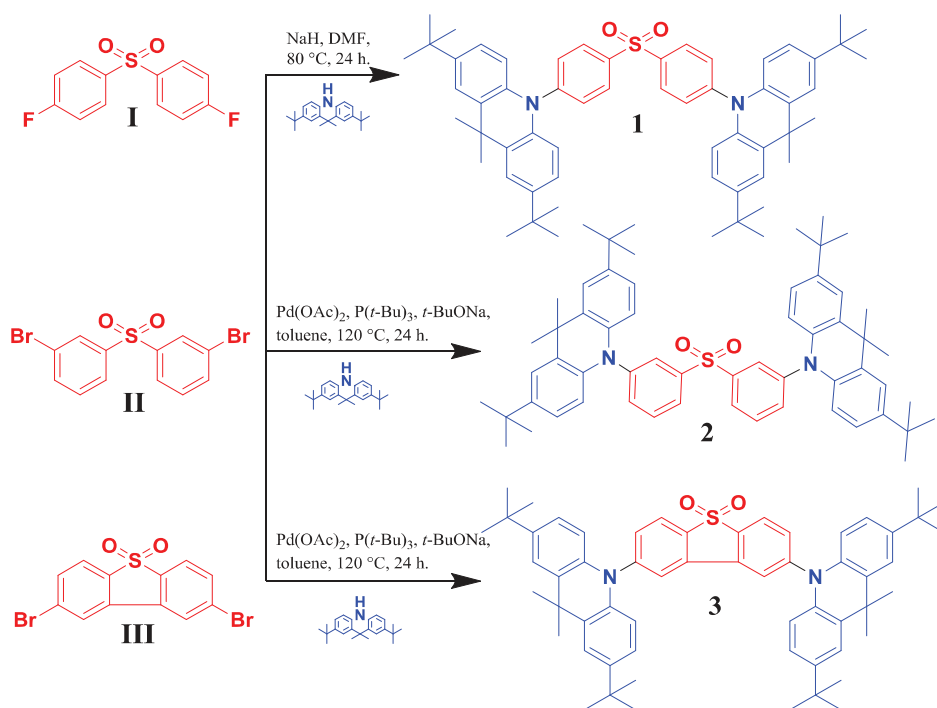
Scheme 1. Synthesis of **1-3.**

2.2.　　　Geometry in the ground and excited electronic states

All the studied molecules **1-3** possess the similar conformational structure in the ground electronic state: both dihydroacridine donor (D) fragments are almost orthogonal with the central

acceptor (A) group (diphenylsulfone for the compounds **1, 2** and dibenzothiophene dioxide for the compound **3** (Figure 1). Dihydroacridine moiety is only slightly twisted along the N-CH2 line because of the sp_3-hybrid carbon atom in the -CH2- link and this effect does not depend on the excitation into the S_1 or T_1 state. The D-A torsion angle is also only slightly dependent on the electronic excitation and is still equivalent for both donors (θ_1 and θ_2 in Figure 1) of compounds **2** and **3**, while for compound **1** the θ_1 angle becomes 26° smaller in the T_1 state comparing with that in the ground singlet state and with the θ_2 angle in the same T_1 state. In the S_1 state of compound **1** both θ_1 and θ_2 angles are still almost equivalent and only slightly larger comparing with the S_0 state. Such behavior of θ_1 and θ_2 angles in the T_1 state can be explained by the high flexibility of the compound **1** due to the absence of sterical hindrance for the mutual rotation of the D-fragments. This derives from the favorable position of dihydroacridine donor in the *para*-positions of the diphenylsulfone acceptor for compound **1** in contrast to the *meta*-substituted compound **2** and rigid-skeleton compound **3**. Actually, compound **1** can be considered as the most flexible system with respect to the mutual rotation between the donor and acceptor moieties, while other the two species are more rigid molecules in this respect.
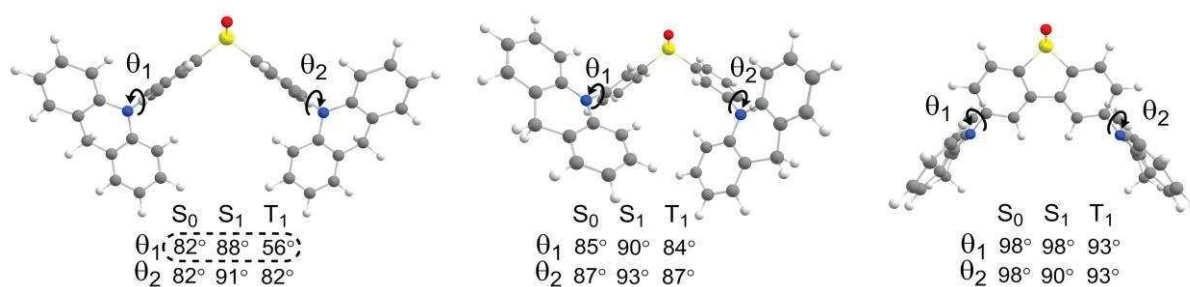

Figure 1. The mutual orientation of donor and acceptor groups for the compounds **1** (left), **2** (middle) and **3** (right) in different electronic states. The *tert*-butyl and methyl groups are omitted for clarify.

2.3. Thermal properties

The temperatures of thermal transitions for derivatives **1-3** were measured by thermogravimetric analysis (TGA) and differential scanning calorimetry (DSC) under nitrogen atmosphere. The information are shown in Table 1. The TGA curves are shown in Supporting Information, see Figure S4). The temperatures of the onsets of thermal degradation of the derivatives were found to be relatively high and ranged from 367 to 416 ºC. It indicates that **1-3** can to be used for device fabrication by vacuum thermal evaporation technology, which can refine the film morphology, and prolong the life time of the devices.

Table 1. Thermal characteristics of derivatives **1-3.**

Derivative	T_m, [ºC][a]	T_g, [°C][b] (2nd heating scan)	T_{cr}, [ºC][c]	T_d^{onset}, [°C][d]
1	-	92	-	416
2	287	126	181	401
3	318	131	182	367

[a] T_m - melting temperature in the second heating (10 °C/min, nitrogen atmosphere). [b] the second heating scan. [b] T_g - glass-transition temperature. [c] T_{cr} - crystallization temperature. [d] T_d^{onset} is the temperature of onset of thermal degradation (20 °C/min, nitrogen atmosphere).

Derivatives **1-3** were excluded after the synthesis as crystalline materials, but they could be reorganized in to molecular glasses by cooling their melts. For example, DSC thermograms of derivative **3** are displayed in Figure 2.
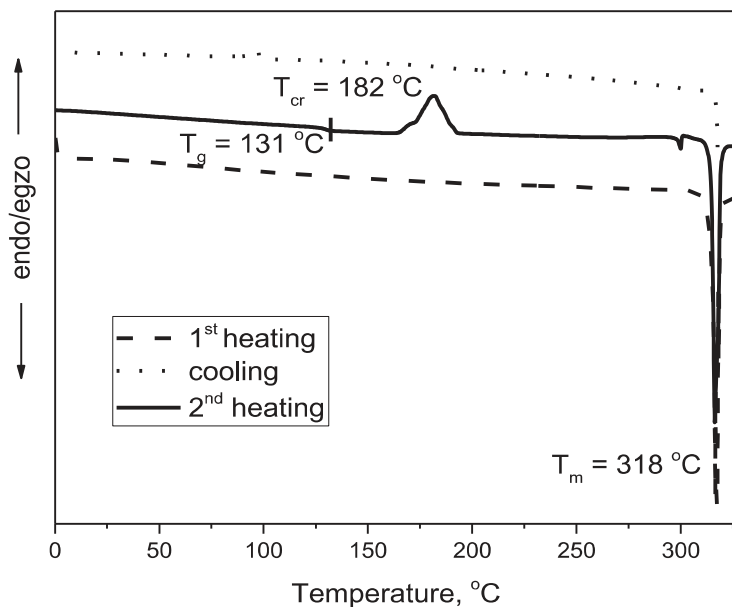
Figure 2. DSC thermograms of compound **3**.

When the probe of **3** was heated during DSC experiment the endothermal melting signal was noticed at 318 °C. The following heating scan revealed signals of glass transition (T_g) at 162 °C, crystallization at 131 °C and melting again at 318 °C. A similar behaviour was observed for compound **2**. In the first heating scan the sample **2** showed an endothermic melting signal at 287 °C. In the second heating scan derivative **2** showed T_g at 126 °C, crystallization at 181 °C and crystallization at 287 °C (see Figure S5). DSC measurements confirmed that the synthesized compound **1** was amorphous material. When sample of **1** was heated, no peaks due to crystallisation and melting appeared. It showed a T_g of 92 °C (see Figure S5). The *meta*-substituted diphenylsulfone **2** exhibited higher T_g by 39 °C compared to *para*-substituted diphenylsulfone **1**. The highest T_g was observed for derivative **3** containing the rigid dibenzothiophene dioxide acceptor unit.

2.4.   Electrochemical and photoelectrical properties

Cyclic voltammetry was employed to investigate electrochemical properties of compounds **1–3**. They showed single oxidation peaks, which can be assigned to the formation of radical cations of the electron-donating *tert*-butylacridanyl moiety (Figure 3a). The compounds showed a close spread of oxidation potentials (0.42-0.45 V). Ionization potential (IP$_{CV}$) values were calculated by the formula $IP_{CV} = |-(1.4 \times 1e^- E^{ox}_{onset} \, vs \, Fc/V) - 4.6| \, eV$ [26]. The data are summarized in Table 2. IP$_{CV}$ values were found to be comarable (5.19 - 5.23 eV). Electron affinities (EA$_{CV}$) estimated using the optical band gaps (E$_g$) and IP$_{CV}$ values were found to range from 3.46 to 3.73 eV. Taking into account that energies of molecular levels are different in solutions and in solid state [27], the ionization potentials (IP$_{EP}$) of the solid layers of **1-3** were additionally estimated by photoelectron emission spectrometry (Figure 3b). Comparable IP$_{EP}$ values of ca. 5.38 eV were obtained for all the derivatives. This observation is thus in good agreement with the cyclic voltammetry data (Table 2). Electron affinities (E_A^{PE}) of 2.25, 2.19, and 2.66 eV for the studied materials **1-3** in solid-state were calculated using the formula $E_A^{PE} = I_P^{PE}$-E_g, where E_g is taken for solid samples (Figure 4a). The IP$_{EP}$ and E_A^{PE} values of solids **1-3** are appropriate for hole and electron injections, respectively. The different substitutions patterns and the different acceptor moieties of compounds **1-3** practically did not affect their energy levels.
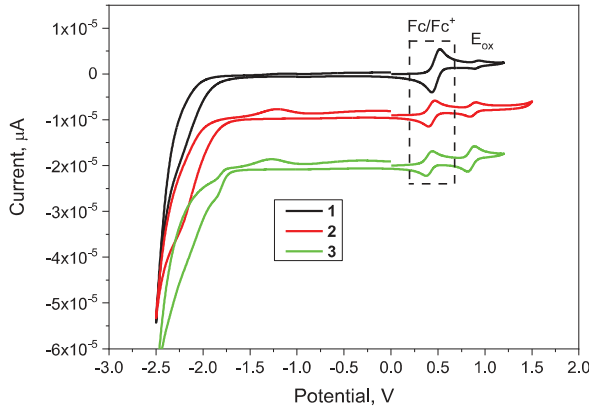
Table 2. Oxidation potential, ionization potentials, electron affinities, and calculated HOMO/LUMO energies of **1-3.**

Derivative	E$^{ox}_{onset}$ *vs* Fc, [V]	IP$_{CV}$[a], HOMO[c] [eV]	EA$_{CV}$[b], LUMO[c] [eV]	I_P^{PE}, [eV][d]	E_A^{PE}, [eV][e]
1	0.42	5.19/-5.21	3.46/-1.75	5.38	2.22

| 2 | 0.44 | 5.22/-5.08 | 3.73/-1.63 | 5.38 | 2.21 |
| 3 | 0.45 | 5.23/-5.25 | 3.69/-2.15 | 5.38 | 2.84 |

[a] $IP_{CV} = |-(1.4 \times 1e^- E_{onset}^{ox} \, vs \, Fc/V) - 4.6| \; eV.$; [b] $EA_{CV} = -(|IP_{CV}| - E_g^{opt})$ E_g^{opt} (E_g^{opt} is onset oxidation potential vs the Fc/Fc$^+$; E_g^{opt} = 1240/λ_{edge}, λ_{edge} is the onset wavelength of absorption spectrum of the dilute THF solution. [c] HOMO and LUMO energies calculated by the B3LYP/6-31G(d) method; [d] I_P^{PE} is the ionization potential of thin solid layers estimated by photoelectron emission spectrometry. [e] E_A^{PE} is electron affinity of thin solid layers estimated by the formula $E_A^{PE} = I_P^{PE} - E_g$. The optical band-gaps (E_g) were taken from absorption spectra of the layers (Figure 4a).

a)   b)
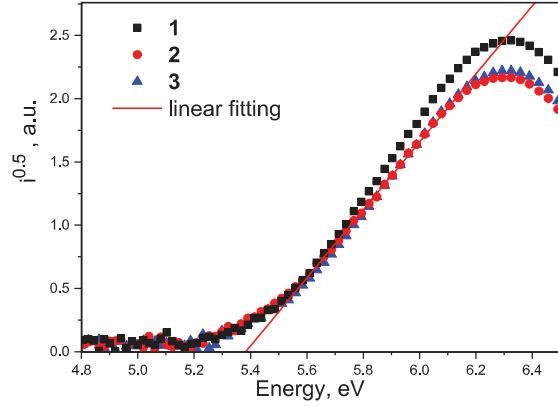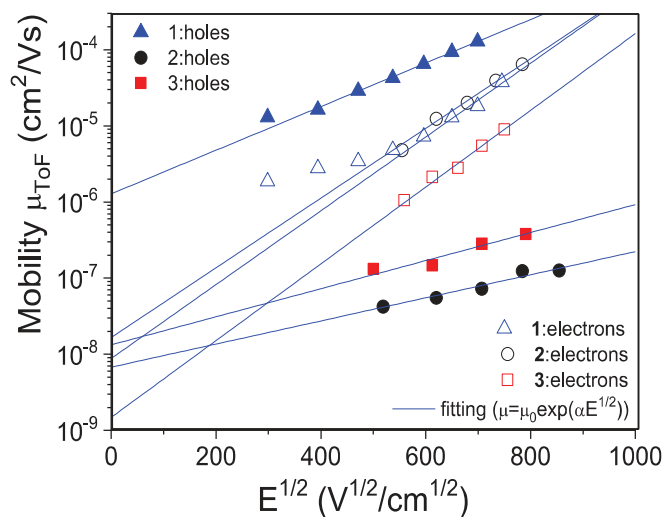
c)

Figure 3. CV curves of dilute solutions of derivatives **1-3** in dichloromethane (100 mV/s) (a); photoelectron emission spectra (b) and electric field dependencies of hole (filled symbols) and electron (empty symbols) drift mobilities (c) for the vacuum-deposited layers of derivatives **1-3**.

The anticipated abilities to transport both holes and electrons were proved for the solid layers of donor-acceptor-donor compounds **1-3** by TOF measurements. Despite highly dispersive charge transport, the transit times (t_{tr}) for both holes and electrons could be obtained by plotting the current transients in the log-log scales (see Figure S5). Thus, t_{tr} was estimated from the intersection points (shown by arrows in Figure S6) at which the asymptotes to the log-log plot crossed. Charge mobility-electric field dependences of the layers of **1-3** well fitted to the Poole–Frenkel relationship $\mu = \mu_0 e^{\alpha E^{1/2}}$, where μ_0 is zero-field electron mobilities, α is the field dependence parameter (the Poole–Frenkel parameter) and E is electric field (Figure 3c) [28]. Such square-root field dependences are usually observed for organic semiconductors [29,30].

11

Close electron mobility values exceeding 3×10^{-5} cm^{2}V^{-1}s^{-1} at electric field higher than 5×10^5 Vcm^{-1} were observed for compounds **1** and **2** containing flexible diphenyl with the same accepting unit diphenylsulfone (Figure 3c). Considerably lower electron mobilities were recorded for compound **3** with rigid dibenzothiophene dioxide unit. Although compounds **1-3** were designed using the same donating units (*tert*-butyl-substituted acridan moiety), very different hole mobilities were observed for their vacuum deposited layers. A hole mobility of 1.3×10^{-4} cm^{2}V^{-1}s^{-1} at electric field of 5×10^5 Vcm^{-1} was observed for the layer of compound **1**, while hole mobilities lower by several orders of magnitude (of 8.1×10^{-8} and 2.6×10^{-7} cm^{2}V^{-1}s^{-1}) were obtained for the layers of compounds **2** and **3**, respectively at the same electric field. This result displays a strong effect of the substitution pattern and of the nature of the acceptor on the hole-transporting properties of the studied compounds. This effect is partly related to different molecular geometry and rigidity of compounds **1-3** which might result in different molecular packing in solid films (Figure 1). Relatively low hole mobilities of compounds **2** and **3** can be apparently explained by weak HOMO-HOMO overlapping of the neighbouring molecules in the solid films. High and relatively balanced hole and electron mobilities of the layers of compound **1** makes it the most promising one for OLED applications.

2.5.   *Photophysical properties*

Photophysical properties of the solutions in the solvents of different polarity as well as of their non-doped and doped films were studied. The low-energy absorption maxima of the solutions of the compounds of their solid films are attributed to the $\pi\rightarrow\pi^*$ transition of the conjugated molecular backbone (Figure 4a). The absorption band with the maximum at *ca.* 286 nm of the

solutions of compounds is apparently related to absorption of acridan. An additional low-energy band at *ca.* 314 nm was observed for the solutions of compound **3**. This band is mainly related to absorption of dibenzothiophene dioxide. Absorption bands which could be attributed to charge transfer (CT) states were practically not observed for dilute solutions of compounds **1-3.** However, absorption tails which can be explained by CT absorption were recorded for the non-doped films of **1-3** (Figure 4a).
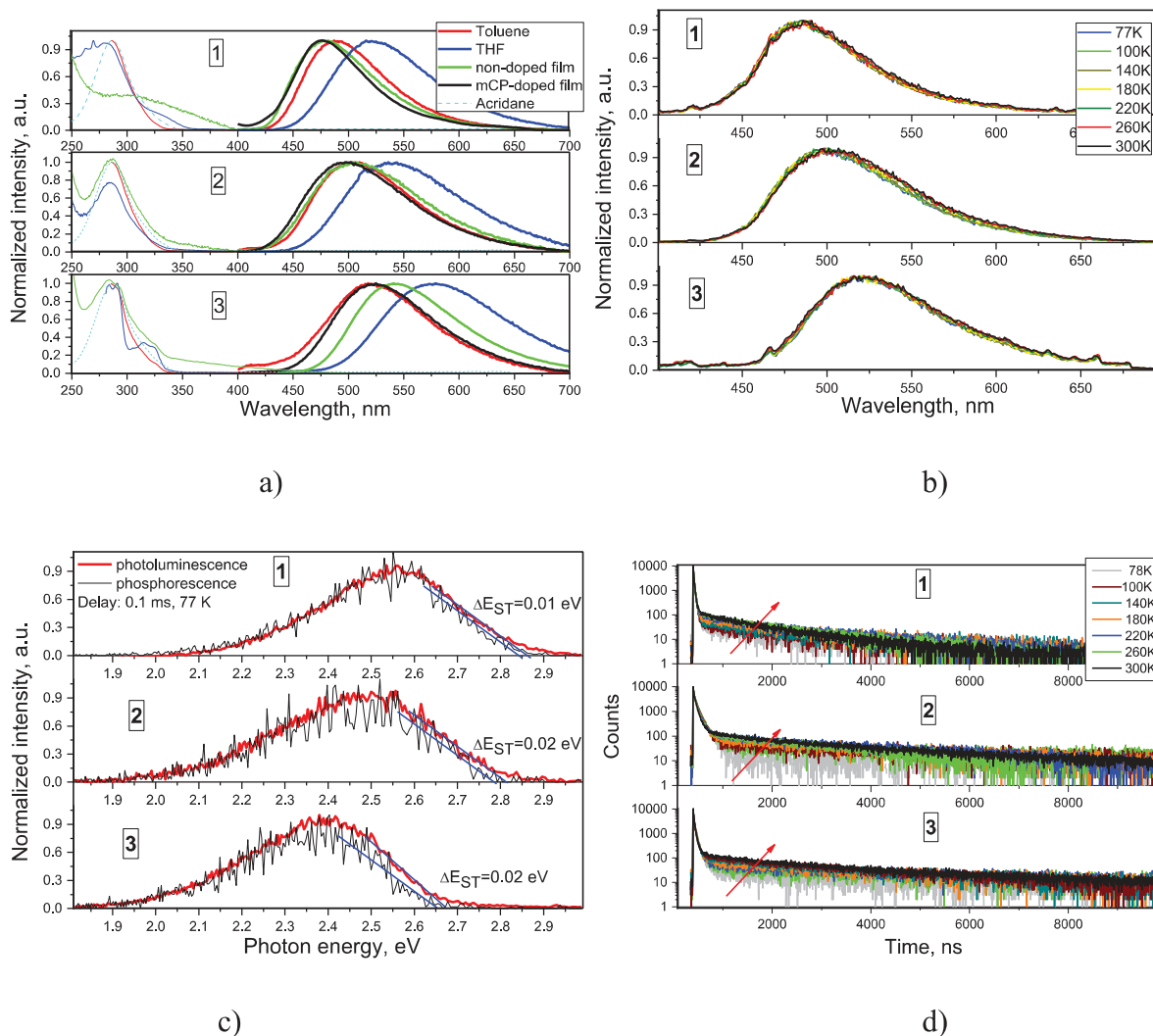

Figure 4. Absorption and PL spectra of the dilute toluene/THF solutions (10^{-5} M) and of non-doped and doped in mCP films for compounds **1-3** (a); PL spectra of the doped films at different

temperatures (b); PL and phosphorescence spectra of the doped films (c); PL decay of doped films recorded at different temperatures.

The solutions of diphenylsulfone-based *para*- and *meta*-substituted compounds **1** and **2** in low-polarity toluene emitted, respectively, blue light with the intensity maximum at 487 nm and sky-blue light with the maximum at 503 nm. Meanwhile, dilute toluene solution of dibenzothiophene dioxide-based compound **3** was characterized by green emission with the maximum at 521 nm. Photoluminescence (PL) spectra of the solutions of compounds **1-3** in more polar THF were red-shifted with respect to those of toluene solutions. Such behaviour is common for donor-acceptor molecules which are characterised by emission with intramolecular CT character [22,31]. In addition to the red-shifts of PL spectra of the THF solutions **1-3**, solvatochromic effect is detected as decreasing emission intensity of THF solutions in comparison to that of the corresponding toluene solutions due to higher polarity of THF. Higher photoluminescence quantum yield (PLQY) values ranging from 5 to 16% (Table 3) were recorded for toluene solutions in comparison to those of the corresponding THF solutions. These PLQY values of air-equilibrated toluene solutions were further increased after deoxygenation.

Table 3. Photophysical parameters derived from steady state, time resolved spectroscopic measurements of dilute solutions and thin films of derivatives **1-3**.

Compounds	λ^{abs}, nm	λ^{PL}, nm	PLQY, %	$\tau_1, \tau_{2,}$[b] ns (χ^2)
	THF	Toluene/THF/film/doped film[a]		
1	282	487/522/475/475	16(20[c])/9/12/55	24, 1782 (1.118)

14

| 2 | 286 | 503/542/502/497 | 5(16[c])/3/3/46 | 63, 3964 (1.255) |
| 3 | 285,315 | 521/577/542/521 | 7(15[c])/4/23/46 | 32, 4642 (1.096) |

[a] mCP was used as the host; [b] PL life times of the doped films; [c] PLQYs given for deoxygenated toluene solutions in parentheses.

Relatively low PLQY values were recorded for non-doped films **1-3** exhibiting aggregation induced quenching (Table 3). However, PLQY values of 55, 46, and 46% were obtained for the doped films, i.e., for 10 wt.% solid solutions of compounds **1-3** in 1,3-bis(*N*-carbazolyl)benzene (mCP). Even these values do not completely display contributions of triplet levels in emission of solid samples since they were tested under air conditions. Because of the polarity effect, the blue-shifted PL spectrum of film of **3** doped in mCP was recorded in comparison to that of the film of net **3**. Unexpectedly, very similar PL spectra were recorded for doped and non-doped films **1**:mCP and **2**:mCP. In addition, PL spectra of non-doped films of compounds **1** and **2** were blue-shifted in comparison to PL spectra of corresponding toluene solutions. Similar unordinary behaviour of emission of TADF emitters in the solid-state was observed for the derivatives of adamantyl-substituted phenyltriazine and 10*H*-spiro[acridine-9,9′-fluorene] [32]. These adamantyl-substituted TADF molecules were designed taking into account the following requirements: **1)** deep HOMO energy level for the donating moiety, **2)** shallow LUMO energy level for the accepting unit, **3)** shallower HOMO of donor than that of acceptor and deeper LUMO of the acceptor than that of the donor for realizing CT, and **4)** locally excited triplet levels (^{3}LE) of both donor and acceptor units higher than CT triplet levels. Being in good agreement with the mentioned requirements,[32] compounds **1** and **2** demonstrated stable emission (non-red-shifted) in their non-doped films. The similar PL spectra of the films of **1-3** doped in mCP were observed in the large range of temperatures from 77 to 300 K (Figure 4b). Such

emission character at different temperatures is possible when the compounds are characterised by practically identical fluorescence and phosphorescence spectra, something that usually is observed at low temperatures (77 K). Indeed, similar fluorescence and phosphorescence spectra were observed by time-resolved PL measurements (Figure 4c). The phosphorescence spectra were recorded using delay of more than 0.1 ms after excitation. The first singlet (S_1) and triplet (T_1) energy levels (marked by straight lines) were taken from the onsets of fluorescence and phosphorescence spectra.

To clearly provide evidence of TADF for compounds **1-3**, fluorescence decay of the films of **1-3** doped in mCP was recorded at different temperatures (Figure 4d). The fluorescence decay curves could be well fitted by a double exponentials with short-lived (τ_1) and long-lived (τ_2) components (Table 3) relating to prompt and delayed fluorescence. Delayed fluorescence of compounds **1-3** is attributed to TADF because the intensity of the fluorescence of their samples progressively rise with the increasing temperature from 77 to 300 K (Figure 4d, shown by arrows).

2.6.   Theoretical background of TADF properties

An important peculiarity of compound **1** (in contrast to compound **2** and **3**) is that its S_1 and T_1 states possess a bi-configurational character. As one can see from Figure 5 both S_1 and T_1 states of compound **1** are composed from two significant configurations, the first configuration with weight ($\nu = 0.829$ and 0.776, respectively) and the second with weight ($\nu = 0.171$ and 0.223, respectively). Both main- and second-weight configurations are actually mirror-equivalent and correspond to the charge-transfer nature of the S_1 and T_1 states (both of $\pi\pi^*$ symmetry). The

SOC between such states of the same symmetry is usually equal to zero or negligibly small (corresponding SOCMEs around 10^{-2}–10^{-3} cm^{-1}) [33,34]. However, the main-weight configuration of the S_1 state and second-weight configuration of the T_1 state are different in orientation (rotation) of the p-AO contribution on the oxygen atoms of the -SO$_2$- group (Figure 5), which implies a significant change of orbital angular momentum moving from S_1 to T_1 state and *vise versa* and which thus provides considerable SOC between these states.[22] Indeed, the $\langle S_1 | \hat{H}_{so} | T_1 \rangle$ SOCME for compound **1** is quite large (0.65 cm^{-1}) that together with the small ΔE_{ST} value (exp.: 0.01 eV, Table 4) provides an efficient and fast rISC. At the same time, compounds **2** and **3** are characterized by the single-configuration S_1 and T_1 states of the same spatial symmetry that correspond to a less efficient SOC between these states (corresponding SOCMEs equal to 0.06 and 0.01 cm^{-1}, respectively, Figure 5) and thus to a less efficient rISC. One can here clearly notice the correlation between the SOCMEs values and EQE values of the final OLEDs (presented in the next section) which supports that the rISC process has a key role and responsible for the high efficiency of light-emitting devices.

From the methodological point of view, one can see that both TDDFT and TDA approaches combined with the tuned range-separated LC-ωPBE functional provides the same high accuracy with respect to the vertical absorption (E_{VA}), vertical emission (E_{VE}) and vertical ΔE_{ST} gap parameters comparing with experimental data. However, adiabatic ΔE_{ST}^{*} gaps are only well reproduced for compound **1**, while for compounds **2** and **3** we observe an artificial (but very small) overestimation of T_1 energy relative to the S_1 reference state. The change of ω parameter in the range 0.13-0.17 does not improve the results, and the usage of the CAM-B3LYP optimized geometries [35] even worsens the resulting ΔE_{ST}^{*} gap. The possible way to improve the ΔE_{ST}^{*} parameter for compounds **2** and **3** is to tune more accurately the ω parameter (by "Golden

proportion" method, for example like in Ref. [36]) or to use alternative functionals or approaches to optimize the S_1 and T_1 geometries.

Table 4. Calculated energies of S_1 state estimated without/with accounting geometry relaxation after excitation and corresponding vertical/adiabatic singlet-triplet gaps in comparison to experimental data for toluene solutions.

Compound		PCM-TD-DFT/LC-ωPBE*/6-31G(d)				PCM-TDA-DFT/LC-ωPBE*/6-31G(d)				Experiment		
	$E_{VA}(S_1)$	$E_{VE}(S_1)$	ΔE_{ST}	ΔE_{ST}^{*}	$E_{VA}(S_1)$	$E_{VE}(S_1)$	ΔE_{ST}	ΔE_{ST}^{*}	$E_{VA}(S_1)$ [a]	$E_{VE}(S_1)$	ΔE_{ST}
1	3.13	2.53	0.02	0.08	3.13	2.53	0.02	0.02	-	2.54	0.01
2	3.19	2.44	0.04	-0.01	3.20	2.44	0.05	-0.01	-	2.47	0.02
3	2.88	2.35	0.02	-0.01	2.89	2.35	0.03	-0.01	-	2.38	0.02

[a] $E_{VA}(S_1)$ can not be extracted from experiment because of very broad, weak and structureless absorption in the low-energy region.

Figure 5. (left) The simplified Jablonski diagram for the compounds **1-3** which explains the TADF principle mediated by the spin-orbit coupling effects through the rISC channel. (right)

18

Natural transition orbital (NTO) pairs for the representative excited states of compounds **1-3**. Hole and particle wave functions with weight ν, are placed above and below the arrows, respectively (insertion). The possible mechanism of SOC between the S_1 and T_1 states of compound **1**.

2.7.   *Electroluminescent performance*

To explores the effects of both rigidity of accepting units and *tert*-butyl modification of donating units on the device efficiencies, different compounds were tested as TADF emitters in the OLEDs. The structures of the TADF OLEDs prepared using compounds **1-3** are shown in Figure 6a. ITO, 50 nm 1,1-bis[*N*,*N*-di(4-tolyl)aminophenyl]cyclohexane (**TAPC**), 10 nm 1,3-bis(*N*-carbazolyl)benzene (**mCP**), 30-nm 9,9'-(2-(1-phenyl-1*H*-benzo[d]imidazol-2-yl)-1,3-phenylene)bis(9*H*-carbazole) (**o-DiCbzBz)** doped with compounds **1-3,** 55 nm diphenylbis[4-(3-pyridyl)phenyl]silane (**DPPS**), 1 nm LiF and 100-nm Al were used for the preparation of the 1[st] hole-transporting layer (HTL), 2[nd] HTL and exciton-blocking layer, emitting layer (EML), electron-transporting layer (ETL), electron-injection layer (EIL) and cathode, respectively [37,38]. As it is visualized in Fig. 6b, the chosen functional layers provided good charge injection into EML. The molecular structures of the organic materials used are shown Figure 6c.
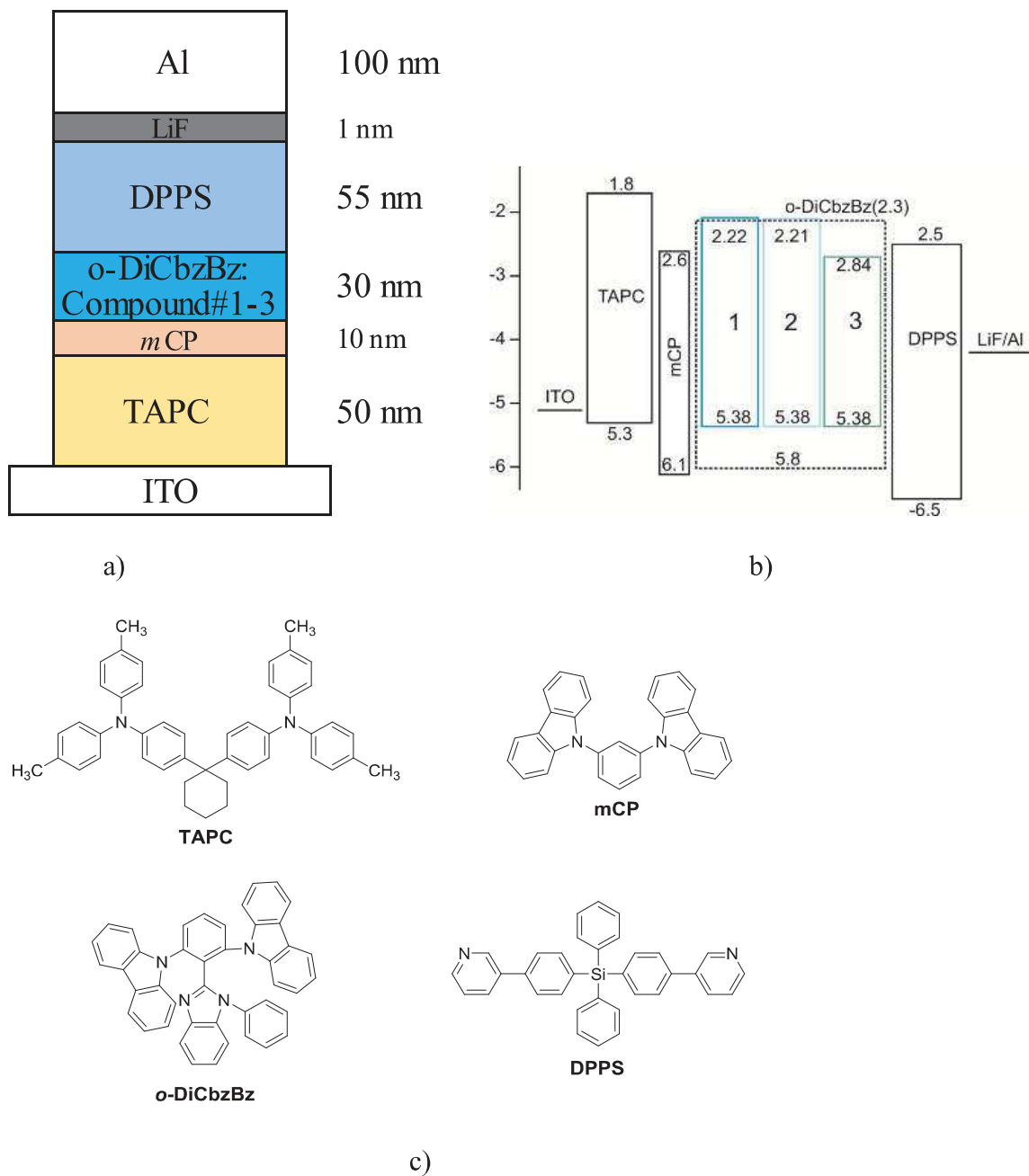
a)

b)

c)

Figure 6. (a) TADF OLED configuration, (b) equilibrium energy diagram, (c) molecular structures of the organic materials used in the devices.

After optimizing the device structure by varying the doping ratio of the compounds and the layer thickness of ETL (results are shown in Figures S7-S10 and Tables S1-S2), the

electroluminescent characteristics of three high-efficiency devices with compound **1-3** were obtained as shown in Figure 7. Except for the doping compound in the EML, the main configuration of these three devices is the same. The dopant concentration is of 24% and ETL layer thickness is of 55 nm. The high dopant concentration of 24% affects the carrier transport and determines the device performance. The device characteristics such as driving voltage at 10 mA/cm^2, maximum CE, PE, EQE, peak wavelength and CIE color coordinates at illuminance of 1000 cd/m^2 are summarized in Table 5. Figure 7a shows their J-V curves. The device with compound **1** exhibits a distinguished J-V behaviour because compound **1** possesses higher charge carrier mobility than compounds **2** and **3** (Figure 3). In addition, this device also performs a stronger illuminance because of the better carrier balance in the EML. The device with compound **2** exhibits a better electrooptical performance than device with compound **3**. This is because compound **2** exhibits a higher electron mobility and a smaller LUMO gap between the *o*-DiCbzBz host and itself to benefit the electron transportation and carrier recombination. The device with compound 1 also shows a distinguished efficiency performance with a CE$_{max}$, PE$_{max}$, and EQE$_{max}$ of 61.1 cdA^{-1}, 64.0 lmW^{-1}, and 24.1%, respectively (Figure 7b). The devices with compound **2** and **3** show a somewhat inferior efficiency. Their emission spectra recorded at a driving voltage of 3.5 V are shown in Figure 7c. Their peak wavelengths locate at 495, 518 and 525 nm with a full width at half maximum (FWHM) of 81, 93 and 86 nm, respectively, corresponding to the CIE coordinates of (0.18, 0.41), (0.26, 0.51), and (0.31, 0.58). The TREL measurements were performed for these three devices for observing their delayed fluorescence by using a PMT detector after device switch off as shown in Figure 7d. The devices showed long emission lifetimes of more than 15 μs, which is delayed fluorescence caused from the triplet excitons rISC to become singlet emission. The device with compound **1** shows much shorter

emission lifetime time. It can be deduced that compound **1** possessed an efficient rISC energy

transfer from T_1 to S_1, which resulted from the smaller ΔE_{ST} (Figure 4c).
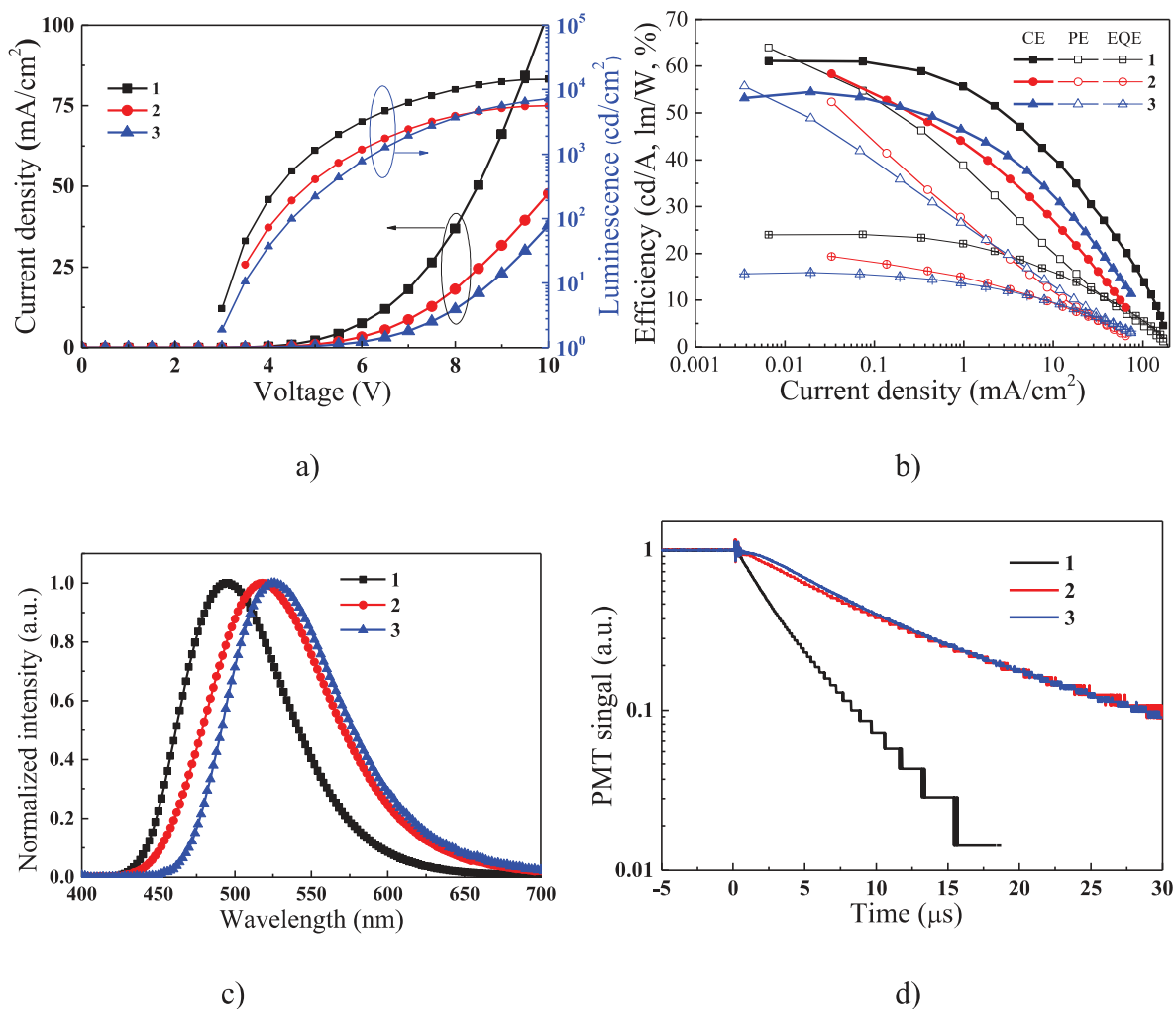

a)

b)

c)

d)

Figure 7. (a) JLV curves, (b) CE, PE and EQE versus J curves, (c) emission spectra at 3.5 V, and

(d) TREL signals of three devices with compounds **1-3** as TADF emitters.

Table 5. Summary of the EL data of devices **1-3.**

Device	Driving voltage (V)[a]	CE_max (cdA^-1)[b]	PE_max (lmW^-1)[b]	EQE_max (%)[b]	Peak wavelength (nm)[c]	CIE (x, y)[d]
1	6.28	61.1	64.0	24.1	495	(0.18, 0.41)
2	7.17	58.4	52.4	19.4	518	(0.26, 0.51)

| **3** | 7.77 | 54.5 | 55.7 | 15.9 | 525 | (0.31, 0.58) |

[a] The operation voltage recorded under current density is 10 mA cm^2. [b] The maximum current efficiency, maximum power efficiency and maximum quantum efficiency. [c] The peak wavelength at 3.5 V driving voltage. [d] The CIE coordinates recorded at a luminance of 1000 cdm^{-2}.

3. Conclusions

Three derivatives containing diphenylsulfone or dibenzothiophene dioxide as acceptor moieties and di-*tert*-butyldimethyldihydroacridine as donor unit were synthesized for use as emitters exhibiting thermally activated delayed fluorescence. Slight modifications in molecular structures resulted in observable differences in thermal, photoelectrical and electroluminescent properties of the compounds. All synthesized compounds exhibited high thermal stability with onsets of thermal degradation ranging from 367 to 416 °C. Moreover, all synthesized compounds were found to be capable of glass formation with glass transition temperatures ranging from 92 to 131 °C. Ionization potentials of the layers of the synthesized compounds were found to be independent on the linking topology and on the nature of acceptor (5.38 eV). The best hole and electron charge-transporting properties were observed for the layers of bis(4-(2,7-di-*tert*-butyl-9,9-dimethyl-9,10-dihydroacridine-10-yl)phenyl)sulfone. A hole mobility of 1.3×10-4 cm^{2}V^{-1}s^{-1} and electron mobility of 3×10^{-5} cm^{2}V^{-1}s^{-1} were recorded for a layer of this compound at an electric field of 5×10^5 Vcm^{-1}. The peaks of the photoluminescence spectra of the compounds were observed at 475, 502 and 542 nm, which correspond to blue, sky-blue and blue-green colour emission. The spectrum of the compound containing a rigid dibenzothiophene dioxide

acceptor unit was red shifted with respect of those of the compounds containing a flexible diphenylsulfone unit. Their small singlet-triplet ΔE_{ST} gaps, ranging from 0.01 to 0.03 eV, guarantees an effective rISC, with an anticipated efficient TADF OLED performance. It was shown that high efficiency of such light-emitting devices is related to existing of bi-configurational nature of the lowest singlet and triplet states of TADF emitter **(1)** with flexible molecular structure resulting in higher spin-orbit coupling between the S_1 and T_1 states and thus in more efficient reverse intersystem crossing comparing to the molecule with rigid acceptor moiety **(3)** of with the close-oriented donor fragments **(2)**. The OLED with *para*-donor-substituted diphenylsulfone as TADF emitter showed a distinct electroluminescent performance with maximum current efficiency, power efficiency and external quantum efficiency of 61.1 cdA^{-1}, 64.0 lmW^{-1}, and 24.1%, respectively. This device showed the shorter lifetime of delayed fluoresce determined by the efficient rISC because of a smaller ΔE_{ST}. Its color coordinates in Commission Internationale de L'Eclairage (CIE) 1931 chromaticity diagram located nearby (0.18, 0.41). Despite both high external quantum efficiency and short electroluminescence lifetime of devices based on TADF emitter **1** with flexible molecular structure, these output OLED parameters were limited by its relatively low PLQYs and "nonoptimal" energy levels. Nevertheless, this work can initiate developments of novel TADF emitters knowing that the "flexibility" is good. The present work represents and translational approach, including rational design and characterization of new high efficiency OLED devices joining quantum mechanical electronic structure calculations, synthetic chemistry, spectroscopy, materials science and device technology. We believe that such an approach has the inherent potential to take further critical steps in the area of OLED technology.

Acknowledgements

Appendix A. Supplementary data

Supplementary data to this article can be found online athttps://doi.org

References

[1]   C.W. Tang, S.A. Vanslyke, Organic electroluminescent diodes, Appl. Phys. Lett. 51 (1987) 913–915. doi:10.1063/1.98799.

[2]   B.W. D'Andrade, S.R. Forrest, White organic light-emitting devices for solid-state lighting, Adv. Mater. 16 (2004) 1585–1595. doi:10.1002/adma.200400684.

[3]   Y.-S. Tyan, Organic light-emitting-diode lighting overview, J. Photonics Energy. 1 (2011) 11009. doi:10.1117/1.3529412.

[4]   Y. Karzazi, Organic light emitting diodes: Devices and applications, J. Mater. Environ. Sci. 5 (2014) 1–12.

[5]   H.-W. Chen, J.-H. Lee, B.-Y. Lin, S. Chen, S.-T. Wu, Liquid crystal display and organic light-emitting diode display: present status and future perspectives, Light Sci. Appl. 7 (2018) 17168–17168. doi:10.1038/lsa.2017.168.

[6]   S.R. Forrest, D.F. O'Brien, Excitonic singlet-triplet ratio in a semiconducting organic thin film, Phys. Rev. B - Condens. Matter Mater. Phys. 60 (1999) 14422–14428. doi:10.1103/PhysRevB.60.14422.

[7]   M.A. Baldo, D.F. O'Brien, Y. You, A. Shoustikov, S. Sibley, M.E. Thompson, S.R. Forrest, Highly efficient phosphorescent emission from organic electroluminescent devices, Nature. 395 (1998) 151–154. doi:10.1038/25954.

[8]   M. Segal, A. Baldo, J. Holmes, R. Forrest, G. Soos, Excitonic singlet-triplet ratios in molecular and polymeric organic materials, Phys. Rev. B - Condens. Matter Mater. Phys. 68 (2003). doi:10.1103/PhysRevB.68.075211.

[9]   A. Endo, M. Ogasawara, A. Takahashi, D. Yokoyama, Y. Kato, C. Adachi, Thermally activated delayed fluorescence from Sn4+-porphyrin complexes and their application to organic light-emitting diodes -A novel mechanism for electroluminescence, Adv. Mater. 21 (2009) 4802–4806. doi:10.1002/adma.200900983.

[10]   H. Uoyama, K. Goushi, K. Shizu, H. Nomura, C. Adachi, Highly efficient organic light-emitting diodes from delayed fluorescence, Nature. 492 (2012) 234–238. doi:10.1038/nature11687.

[11]   M. Yokoyama, K. Inada, Y. Tsuchiya, H. Nakanotani, C. Adachi, Trifluoromethane modification of thermally activated delayed fluorescence molecules for high-efficiency blue organic light-emitting diodes, Chem. Commun. 54 (2018) 8261–8264. doi:10.1039/c8cc03425g.

[12]   Q. Zhang, J. Li, K. Shizu, S. Huang, S. Hirata, H. Miyazaki, C. Adachi, Design of efficient thermally activated delayed fluorescence materials for pure blue organic light emitting diodes, J. Am. Chem. Soc. 134 (2012) 14706–14709. doi:10.1021/ja306538w.

[13]   D.R. Lee, M. Kim, S.K. Jeon, S.H. Hwang, C.W. Lee, J.Y. Lee, Design strategy for 25% external quantum efficiency in green and blue thermally activated delayed fluorescent devices, Adv. Mater. 27 (2015) 5861–5867. doi:10.1002/adma.201502053.

[14]   Y. Liu, C. Li, Z. Ren, S. Yan, M.R. Bryce, All-organic thermally activated delayed fluorescence materials for organic light-emitting diodes, Nat. Rev. Mater. 3 (2018) 1-20. doi:10.1038/natrevmats.2018.20.

[15]   T. Hosokai, H. Matsuzaki, H. Nakanotani, K. Tokumaru, T. Tsutsui, A. Furube, K. Nasu, H. Nomura, M. Yahiro, C. Adachi, Evidence and mechanism of efficient thermally activated delayed fluorescence promoted by delocalized excited states, Sci. Adv. 3 (2017) e1603282/1–9. doi:10.1126/sciadv.1603282.

[16]   O. Bezvikonnyi, D. Gudeika, D. Volyniuk, V. Mimaite, B.R. Sebastine, J. V. Grazulevicius, Effect of donor substituents on thermally activated delayed fluorescence of diphenylsulfone derivatives, J. Lumin. 206 (2019) 250–259. doi:10.1016/j.jlumin.2018.10.018.

[17]   M.Y. Wong, E. Zysman-Colman, Adv. Mater., 29 (2017) 1605444. doi.org/10.1002/adma.201605444.

[18]   J. Hu, Q. Li, X. Wang, S. Shao, L. Wang, X. Jing, F. Wang, Developing through-space charge transfer polymers as a general approach to realize full-color and white emission with

thermally activated delayed fluorescence, Angew. Chemie - Int. Ed. 58 (2019) 8405–8409. doi:10.1002/anie.201902264.

[19]   D. Zhang, X. Song, M. Cai, H. Kaji, L. Duan, Versatile indolocarbazole-isomer derivatives as highly emissive emitters and ideal hosts for thermally activated delayed fluorescent OLEDs with alleviated efficiency roll-off, Adv. Mater. 30 (2018) 1705250. doi:10.1002/adma.201705406.

[20]   C. Li, C. Duan, C. Han, H. Xu, Secondary acceptor optimization for full-exciton radiation: Toward sky-blue thermally activated delayed fluorescence diodes with external quantum efficiency of ≈30%, Adv. Mater. 30 (2018) 1804228. doi:10.1002/adma.201804228.

[21]   C.Y. Chan, L.S. Cui, J.U. Kim, H. Nakanotani, C. Adachi, Rational molecular design for deep-blue thermally activated delayed fluorescence emitters, Adv. Funct. Mater. 28 (2018) 1706023. doi:10.1002/adfm.201706023.

[22]   Y. Im, S.H. Han, J.Y. Lee, Deep blue thermally activated delayed fluorescent emitters using CN-modified indolocarbazole as an acceptor and carbazole-derived donors, J. Mater. Chem. C. 6 (2018) 5012–5017. doi:10.1039/c8tc00546j.

[23]   B. Huang, Q. Qi, W. Jiang, J. Tang, Y. Liu, W. Fan, Z. Yin, F. Shi, X. Ban, H. Xu, Y. Sun, Thermally activated delayed fluorescence materials based on 3,6-di-tert-butyl-9-((phenylsulfonyl)phenyl)-9H-carbazoles, Dye. Pigment. 111 (2014) 135–144. doi:10.1016/j.dyepig.2014.06.008.

[24]   C.R. Neumoyer, E.D. Amstutz, Studies in the Sulfone Series. I. The preparation of 2,8-diaminodibenzothiophene-5-dioxide, J. Am. Chem. Soc. 69 (1947) 1920–1921. doi:10.1021/ja01200a023.

25   K. Yofu, K. Nomura, E. Fukuzaki, Y. Hirai, M. Hamano, T. Mitsui, United States Patent US9349965, 2016.

[26]   B.W. D'Andrade, S. Datta, S.R. Forrest, P. Djurovich, E. Polikarpov, M.E. Thompson, Relationship between the ionization and oxidation potentials of molecular organic semiconductors, Org. Electron. Physics, Mater. Appl. 6 (2005) 11–20. doi:10.1016/j.orgel.2005.01.002.

[27]   J. Sworakowski, How accurate are energies of HOMO and LUMO levels in small-molecule organic semiconductors determined from cyclic voltammetry or optical spectrosco, Synth. Met. 235 (2018) 125–130. doi:10.1016/j.synthmet.2017.11.013.

[28]   V.I. Arkhipov, I.I. Fishchuk, A. Kadashchuk, H. Bassler, ed. G. Lanzani, Wiley VCH Verlag GmbH & Co. KGaA, Weinheim, ch. 6 (2006) 350–356.

[29]   L. Li, S. Van Winckel, J. Genoe, P. Heremans, Electric field-dependent charge transport in organic semiconductors, Appl. Phys. Lett. 95 (2009) 153301-1-3. doi:10.1063/1.3246160.

[30]   C.Y.H. Chan, K.K. Tsung, W.H. Choi, S.K. So, Achieving time-of-flight mobilities for amorphous organic semiconductors in a thin film transistor configuration, Org. Electron. Physics, Mater. Appl. 14 (2013) 1351–1358. doi:10.1016/j.orgel.2013.02.007.

[31]   Z. He, X. Cai, Z. Wang, Y. Li, Z. Xu, K. Liu, D. Chen, S.J. Su, Sky-blue thermally activated delayed fluorescence material employing a diphenylethyne acceptor for organic light-emitting diodes, J. Mater. Chem. C. 6 (2017) 36–42. doi:10.1039/c7tc02763j.

[32]   Y. Wada, S. Kubo, H. Kaji, Adamantyl substitution strategy for realizing solution-processable thermally stable deep-blue thermally activated delayed fluorescence materials, Adv. Mater. 30 (2018). doi:10.1002/adma.201705641.

[33]   P.K. Samanta, D. Kim, V. Coropceanu, J.L. Brédas, Up-conversion intersystem crossing rates in organic emitters for thermally activated delayed fluorescence: Impact of the nature of singlet vs triplet excited states, J. Am. Chem. Soc. 139 (2017) 4042–4051. doi:10.1021/jacs.6b12124.

[34]   G. Baryshnikov, B. Minaev, H. Ågren, Theory and calculation of the phosphorescence phenomenon, Chem. Rev. 117 (2017) 6500–6537. doi:10.1021/acs.chemrev.7b00060.

[35]   T. Yanai, D.P. Tew, N.C. Handy, A new hybrid exchange-correlation functional using the Coulomb-attenuating method (CAM-B3LYP), Chem. Phys. Lett. 393 (2004) 51–57. doi:10.1016/j.cplett.2004.06.011.

[36]   H. Sun, C. Zhong, J.L. Brédas, Reliable Prediction with tuned range-separated functionals of the singlet-triplet gap in organic emitters for thermally activated delayed fluorescence, J. Chem. Theory Comput. 11 (2015) 3851–3858. doi:10.1021/acs.jctc.5b00431.

[37]   J.J. Huang, Y.H. Hung, P.L. Ting, Y.N. Tsai, H.J. Gao, T.L. Chiu, J.H. Lee, C.L. Chen, P.T. Chou, M.K. Leung, Orthogonally substituted benzimidazole-carbazole benzene as universal hosts for phosphorescent organic light-emitting diodes, Org. Lett. 18 (2016) 672–675. doi:10.1021/acs.orglett.5b03631.

[38]   Y.T. Lee, P.C. Tseng, T. Komino, M. Mamada, R.J. Ortiz, M.K. Leung, T.L. Chiu, C.F. Lin, J.H. Lee, C. Adachi, C.T. Chen, C.T. Chen, Simple molecular-engineering approach for enhancing orientation and outcoupling efficiency of thermally activated delayed fluorescent emitters without red-shifting emission, ACS Appl. Mater. Interfaces. 10 (2018) 43842–43849. doi:10.1021/acsami.8b16199.
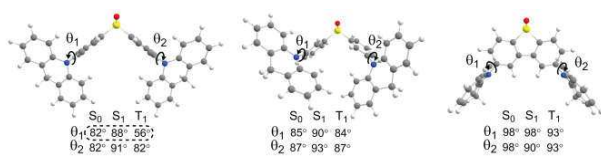
Figure 1

Figure 1. The mutual orientation of donor and acceptor groups for the compounds **1** (left), **2** (middle) and **3** (right) in different electronic states. The *tert*-butyl and methyl groups are omitted for clarify.
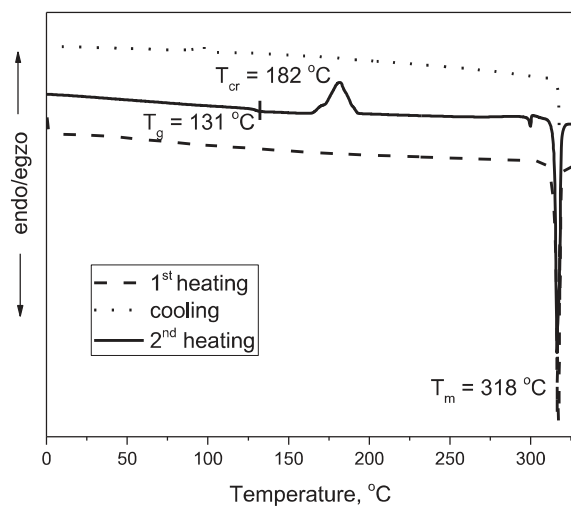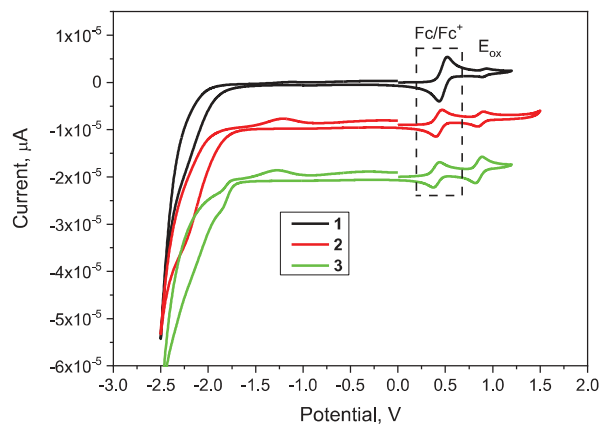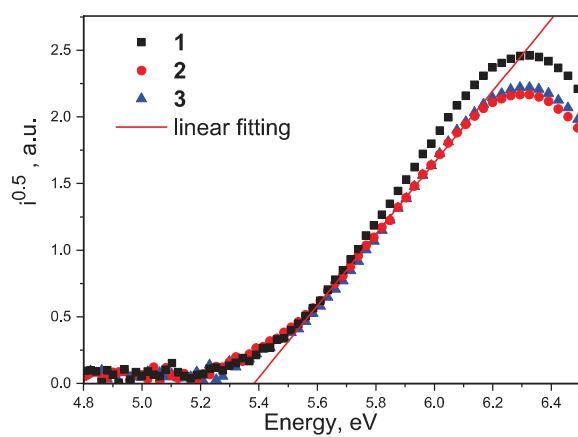
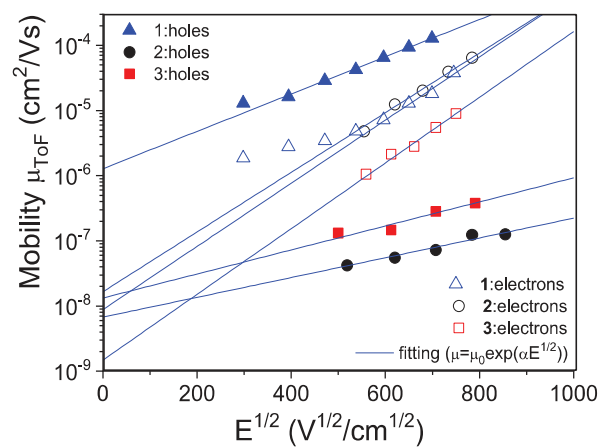**Figure 2**

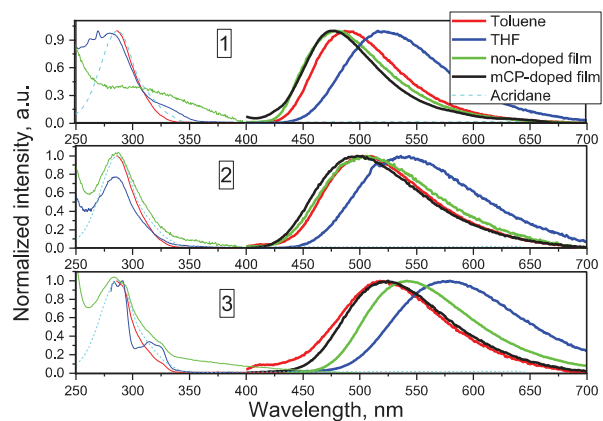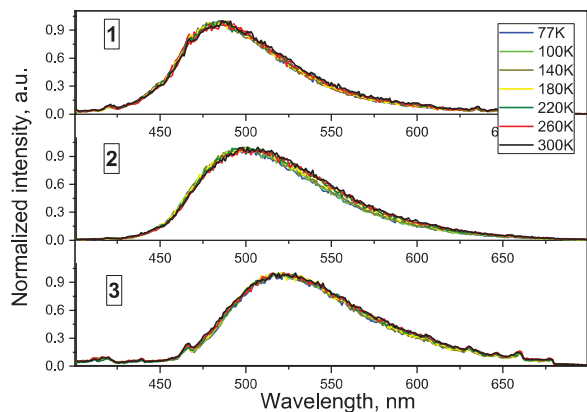**Figure 2.** DSC thermograms of compound **3**.
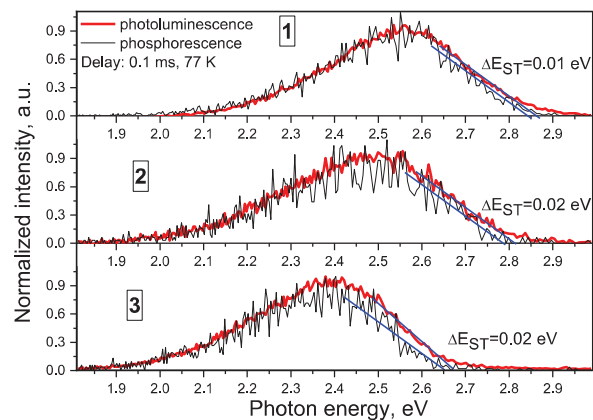
Figure 3

a)

b)

c)

Figure 3. CV curves of dilute solutions of derivatives **1-3** in dichloromethane (100 mV/s) (a); photoelectron emission spectra (b) and electric field dependencies of hole (filled symbols) and electron (empty symbols) drift mobilities (c) for the vacuum-deposited layers of derivatives **1-3**.
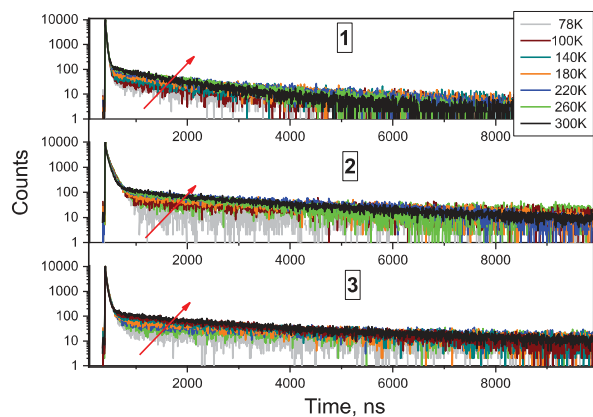
Figure 4

a)

b)

c)

d)

Figure 4. Absorption and PL spectra of the dilute toluene/THF solutions (10^{-5} M) and of non-doped and doped in mCP films for compounds **1-3** (a); PL spectra of the doped films at different temperatures (b); PL and phosphorescence spectra of the doped films (c); PL decay of doped films recorded at different temperatures.
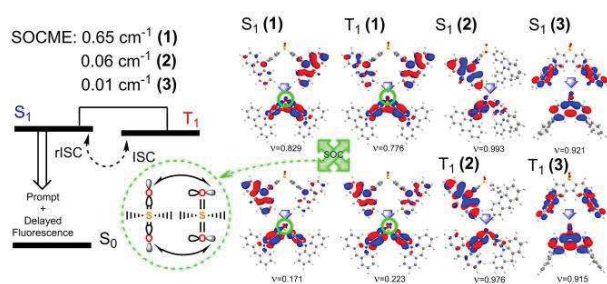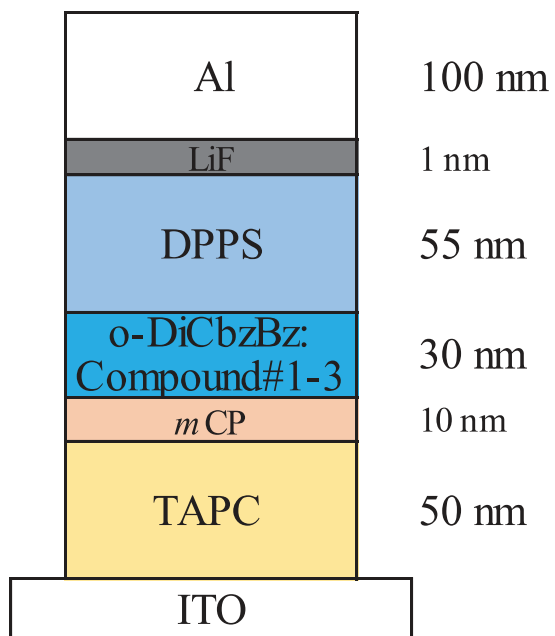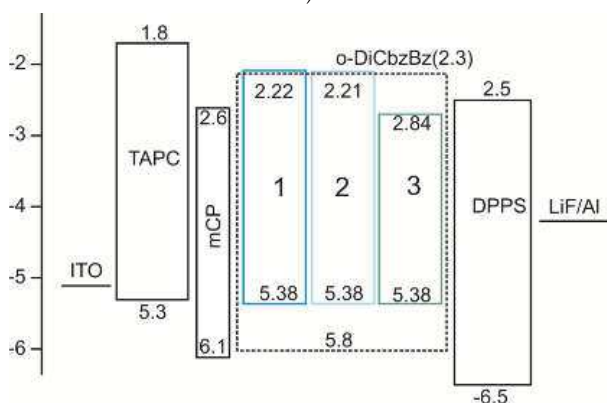
Figure 5

Figure 5. (left) The simplified Jablonski diagram for the compounds **1-3** which explains the TADF principle mediated by the spin-orbit coupling effects through the rISC channel. (right) Natural transition orbital (NTO) pairs for the representative excited states of compounds **1-3**. Hole and particle wave functions with weight v, are placed above and below the arrows, respectively (insertion). The possible mechanism of SOC between the S_1 and T_1 states of compound **1**.
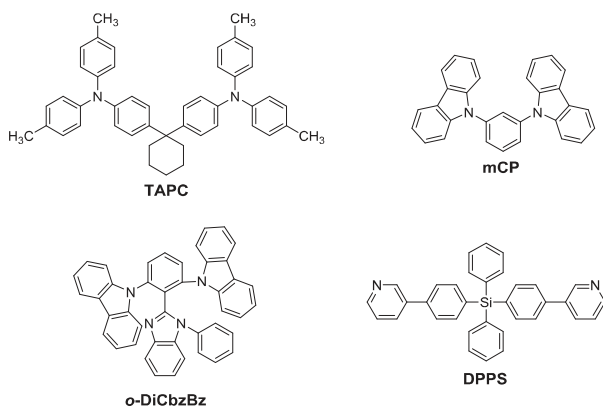
Figure 6

a)

b)

c)

Figure 6. (a) TADF OLED configuration, (b) equilibrium energy diagram, (c) molecular structures of the organic materials used in the devices.
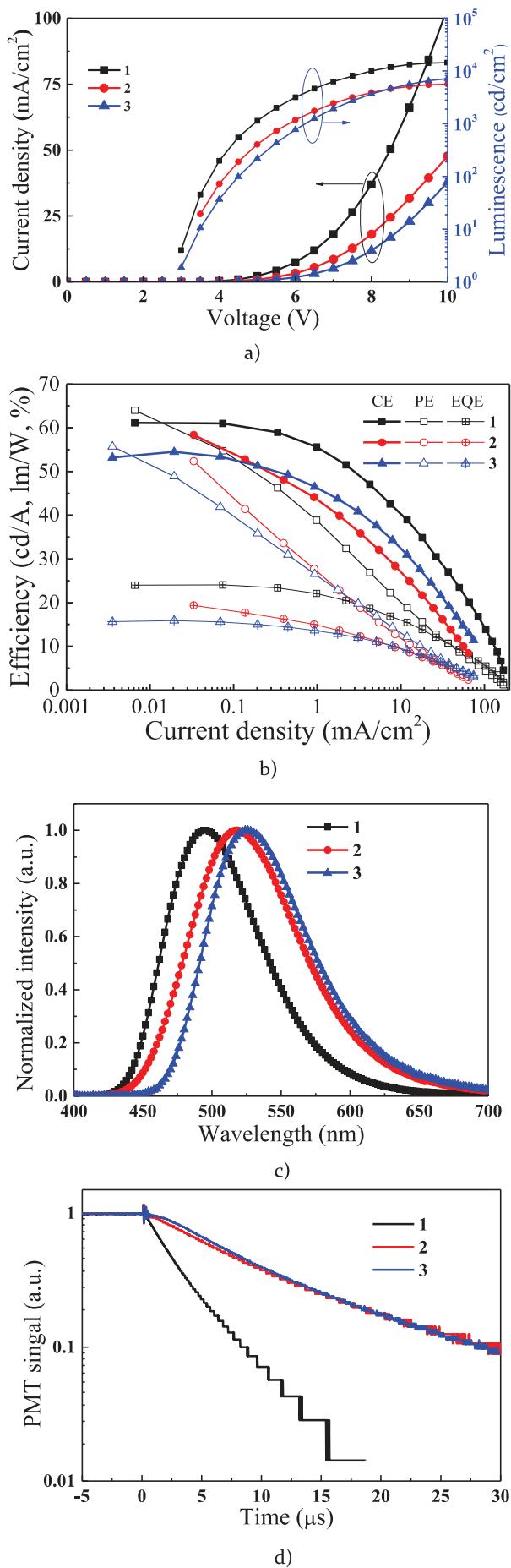
Figure 7

a)

b)

c)

d)

Figure 7. (a) JLV curves, (b) CE, PE and EQE versus J curves, (c) emission spectra at 3.5 V, and (d) TREL signals of three devices with compounds **1-3** as TADF emitters.

Table 1

Table 1. Thermal characteristics of derivatives **1-3.**

Derivative	T_m, [°C][a]	T_g, [°C][b] (2nd heating scan)	T_{cr}, [°C][c]	T_d^{onset}, [°C][d]
1	-	92	-	416
2	287	126	181	401
3	318	131	182	367

[a] T_m - melting temperature in the second heating (10 °C/min, nitrogen atmosphere). [b] the second heating scan. [b] T_g - glass-transition temperature. [c] T_{cr} - crystallization temperature. [d] T_d^{onset} is the temperature of onset of thermal degradation (20 °C/min, nitrogen atmosphere).

Table 2

Table 2. Oxidation potential, ionization potentials, electron affinities, and calculated HOMO/LUMO energies of **1-3.**

Derivative	E^{ox}_{onset} vs Fc, [V]	IP_{CV}[a], HOMO[c] [eV]	EA_{CV}[b], LUMO[c] [eV]	$I_P{}^{PE}$, [eV][d]	$E_A{}^{PE}$, [eV][e]
1	0.42	5.19/-5.21	3.46/-1.75	5.38	2.22
2	0.44	5.22/-5.08	3.73/-1.63	5.38	2.21
3	0.45	5.23/-5.25	3.69/-2.15	5.38	2.84

[a] $IP_{CV} = |-(1.4 \times 1e^- E^{ox}_{onset}\ vs\ Fc/V) - 4.6|\ eV.$; [b] $EA_{CV} = -(|IP_{CV}| - E_g^{opt})$ (E_g^{opt} is onset oxidation potential vs the Fc/Fc$^+$; $E_g^{opt} = 1240/\lambda_{edge}$, λ_{edge} is the onset wavelength of absorption spectrum of the dilute THF solution. [c] HOMO and LUMO energies calculated by the B3LYP/6-31G(d) method; [d] $I_P{}^{PE}$ is the ionization potential of thin solid layers estimated by photoelectron emission spectrometry. [e] $E_A{}^{PE}$ is electron affinity of thin solid layers estimated by the formula $E_A{}^{PE} = I_P{}^{PE} - E_g$. The optical band-gaps (E_g) were taken from absorption spectra of the layers (Figure 4a).

Table 3

Table 3. Photophysical parameters derived from steady state, time resolved spectroscopic measurements of dilute solutions and thin films of derivatives **1-3.**

Compounds	λ^{abs}, nm	λ^{PL}, nm	PLQY, %	τ_1, τ_2,[b] ns (χ^2)
	THF	Toluene/THF/film/doped film[a]		
1	282	487/522/475/475	16(20[c])/9/12/55	24, 1782 (1.118)
2	286	503/542/502/497	5(16[c])/3/3/46	63, 3964 (1.255)
3	285,315	521/577/542/521	7(15[c])/4/23/46	32, 4642 (1.096)

[a] mCP was used as the host; [b] PL life times of the doped films; [c] PLQYs given for deoxygenated toluene solutions in parentheses.

Table 4

Table 4. Calculated energies of S_1 state estimated without/with accounting geometry relaxation after excitation and corresponding vertical/adiabatic singlet-triplet gaps in comparison to experimental data for toluene solutions.

Compound	PCM-TD-DFT/LC-ωPBE*/6-31G(d)				PCM-TDA-DFT/LC-ωPBE*/6-31G(d)				Experiment		
	$E_{VA}(S_1)$	$E_{VE}(S_1)$	ΔE_{ST}	ΔE_{ST}^*	$E_{VA}(S_1)$	$E_{VE}(S_1)$	ΔE_{ST}	ΔE_{ST}^*	$E_{VA}(S_1)$ [a]	$E_{VE}(S_1)$	ΔE_{ST}
1	3.13	2.53	0.02	0.08	3.13	2.53	0.02	0.02	-	2.54	0.01
2	3.19	2.44	0.04	-0.01	3.20	2.44	0.05	-0.01	-	2.47	0.02
3	2.88	2.35	0.02	-0.01	2.89	2.35	0.03	-0.01	-	2.38	0.02

[a] $E_{VA}(S_1)$ can not be extracted from experiment because of very broad, weak and structureless absorption in the low-energy region.

Table 5

Table 5. Summary of the EL data of devices **1-3.**

Device	Driving voltage (V)[a]	CE$_{max}$ (cdA^{-1})[b]	PE$_{max}$ (lmW^{-1})[b]	EQE$_{max}$ (%)[b]	Peak wavelength (nm)[c]	CIE (x, y)[d]
1	6.28	61.1	64.0	24.1	495	(0.18,0.41)
2	7.17	58.4	52.4	19.4	518	(0.26,0.51)
3	7.77	54.5	55.7	15.9	525	(0.31,0.58)

[a] The operation voltage recorded under current density is 10 mA cm^2. [b] The maximum current efficiency, maximum power efficiency and maximum quantum efficiency. [c] The peak wavelength at 3.5 V driving voltage. [d] The CIE coordinates recorded at a luminance of 1000 cdm^{-2}.